

Journal of Biomedical Optics

SPIEDigitalLibrary.org/jbo

Complex conjugate artifact-free adaptive optics optical coherence tomography of *in vivo* human optic nerve head

Dae Yu Kim
John S. Werner
Robert J. Zawadzki

Complex conjugate artifact-free adaptive optics optical coherence tomography of *in vivo* human optic nerve head

Dae Yu Kim, John S. Werner, and Robert J. Zawadzki

University of California Davis Eye Center, Vision Science and Advanced Retinal Imaging Laboratory, 4860 Y Street, Suite 2400, Sacramento, California 95817

Abstract. We acquired *in vivo* images of the human optic nerve head (ONH) using an adaptive optics—optical coherence tomography (AO-OCT) system. In order to improve imaging of the lamina cribrosa in the ONH with high lateral resolution and sensitivity, we implemented a complex conjugate artifact-free Fourier domain OCT (Fd-OCT) acquisition scheme with a reference arm-based phase shifting method. This allowed positioning of the lamina cribrosa structures near the zero path length difference where AO-OCT imaging achieves highest sensitivity. Implementation of our complex conjugate artifact removal (CCR) method required constant phase shifts between consecutive axial scans (A-scans), generated by continuous beam path-length changes from offsetting the pivot point of the scanning mirror placed in the reference arm. Fourier transform along the transverse axis and a filtering algorithm allowed reconstruction of CCR AO-OCT images. The suppression ratio of the mirror artifact was approximately 22 dB (at 18,000 A-scans per second acquisition speed) with a paperboard test target and an optimum phase-shift value. Finally, we reconstructed the three-dimensional structure of human ONH with enhanced depth range and sensitivity using CCR AO-OCT. © 2012 Society of Photo-Optical Instrumentation Engineers (SPIE). [DOI: [10.1117/1.JBO.17.12.126005](https://doi.org/10.1117/1.JBO.17.12.126005)]

Keywords: adaptive optics; optical coherence tomography; ophthalmology; imaging systems; medical optics instrumentation; aberration compensation; complex conjugate artifact.

Paper 12410P received Jul. 3, 2012; revised manuscript received Oct. 18, 2012; accepted for publication Oct. 31, 2012; published online Dec. 3, 2012.

1 Introduction

Fourier domain, or spectral domain, optical coherence tomography (Fd-OCT)^{1,2} inherently produces complex conjugate images (two identical images) after Fourier transform of the acquired spectral fringe signal from the spectrometer. Almost all Fd-OCT systems display only one side of the Fourier space, called a real or a true image, and require that the imaged structure is placed on a positive or a negative path length difference side. However, there exists an identical image, called a mirror or a complex conjugate artifact image, in the opposite side of the Fourier space. A complex conjugate artifact removed image would allow the location of the imaged structure to be at any position with respect to the zero path length difference, doubling the available axial imaging range and hence the name “full-range” imaging in Fd-OCT.

Complex conjugate removal (CCR) in Fd-OCT allows the ocular structure of interest to be placed close to the zero path length difference achieving maximum system sensitivity. Additionally one does not need to monitor axial position of the sample during imaging because there is no artifact generated if the structure crosses the zero path length difference position. For these reasons, we previously investigated strategies to increase the axial depth range of the Fd-OCT by removal of the complex conjugate ambiguity in the Fourier-transformed data.³ The common theme of the complex conjugate artifact removal

techniques focuses on reconstructing the complex representation of the “real” spectral fringes acquired by the OCT detector. Several reconstruction approaches with a phase shifting method,⁴ a piezoelectric actuator (PZT),⁵ and a dispersion encoded algorithm⁶ were developed to achieve mirror artifact-free images in Fd-OCT. A recent work demonstrated complex conjugate ambiguity-free images of human ocular anterior segments acquired with swept-source OCT using phase modulation created by the swept-source laser without the use of any external device.⁷ Currently, the use of the swept light source for adaptive optics-optical coherence tomography (AO-OCT) is limited due to relatively low axial resolution (about 10 μm) offered by commercial swept laser sources, if compared to broadband superluminescent diodes (axial resolution up to 2 μm), the most commonly used light source for spectrometer-based OCT systems.

One potentially attractive application of CCR AO-OCT is *in vivo* optic nerve head (ONH) and lamina cribrosa imaging. Due to the relatively large axial extent of ONH structure, one can observe degradation in intensity of the structures located further away from the zero path length difference position. This effect is independent from simple optical focusing and is due to sensitivity roll-off in spectrometer-based Fd-OCT systems.⁸ In order to limit this effect and to allow optimal imaging of the structure of interest, we implemented the CCR method allowing axial positioning of the structure of interest near the zero path length difference position without the presence of complex conjugate mirror artifacts. According to an ONH

Address all correspondence to: Robert J. Zawadzki, University of California Davis Eye Center, Vision Science and Advanced Retinal Imaging Laboratory, 4860 Y Street, Suite 2400, Sacramento, California 95817. Tel: 916-734-4541; Fax: 916-734-4543; E-mail: rjzawadzki@ucdavis.edu

0091-3286/2012/\$25.00 © 2012 SPIE

topology study,⁹ the average maximum cup depth of 100 normal human subjects is 0.621 mm. Sensitivity drop of our AO-OCT system at 0.6 mm away from the zero path length difference is 6 dB. In standard OCT imaging, thus, the ONH cup has to be placed at least 0.6 mm away from the zero path length difference in order to avoid overlapping real and mirror images of an ONH structure in Fd-OCT.

For an AO-OCT imaging system, the usable depth range is further limited to the area where the lateral resolution is high. Thus, with eye pupil diameters used for AO imaging and in the diffraction-limited case, depth of focus of the imaging beam is $<100\ \mu\text{m}$ (about 3 to 4 times lower than retinal thickness) and multiple imaging of a single location with different position of the focus would be necessary to have optimum lateral resolution of all retinal structures. Increasing the axial range and removal of the complex conjugate artifact in AO-OCT is nevertheless important in evaluating changes in the optic nerve head including lamina cribrosa for study of optic neuropathies, where the “accessible” axial range should be on the order of 2 mm.

The lamina cribrosa located inside the ONH is made of a mesh-like multilayered volumetric porous network of collagen fibers. This is the exit canal where ganglion cell axons form the optic nerve and where the major blood vessels (the central retinal artery and vein) that supply the retina enter the eye. Primate eye studies have demonstrated that morphological changes of this area by mechanical stresses, including elevated intra-ocular pressure, could cause loss of axonal density¹⁰ or deficits of blood flow to the anterior optic nerve¹¹ associated with glaucoma.

Damage to the retinal ganglion cells and their axons in glaucoma can be identified by structural abnormalities of the ONH. For example, changes have been measured in the optic disk size, rim area, and cup-disk area ratio with fundus photography and the confocal scanning laser ophthalmoscope.¹² Deformation of structures in the lamina cribrosa have also been described, but three-dimensional *in vivo* visualization of lamina cribrosa or optic nerve head morphology is limited for diagnosis and treatment monitoring. *En face* images obtained with adaptive optics scanning laser ophthalmoscopy (AO-SLO) demonstrated lamina pores of glaucomatous eyes from the rhesus monkey.¹³ Recently, lamina pore areas from normal subjects¹⁴ and glaucoma patients¹⁵ have been measured *in vivo* with AO-SLO. Volumetric porous structures of the lamina cribrosa with healthy subjects^{16,17} and ocular hypertension as well as glaucoma patients¹⁸ have been demonstrated using OCT. In addition, we presented high-resolution images of ONH and lamina cribrosa with high axial and lateral resolution using CCR AO-OCT.¹⁹

In this manuscript, we implemented a complex conjugate removal method in our AO-OCT system using reference arm–based phase shifting. For the first time, we reconstructed complex conjugate ambiguity-free AO-OCT images with high lateral resolution and an enhanced depth range. As a potential application of this technique, we demonstrated ONH (lamina cribrosa) imaging of a healthy volunteer. *In vivo* lamina pore areas from reconstructed *en face* views were measured as well.

2 Materials and Methods

Complex conjugate artifact-free AO-OCT images of *in vivo* human optic nerve head were acquired from a healthy 60-year-old volunteer. Figure 1(a) shows a color fundus photograph of the left eye of the subject acquired with a Topcon TRC-50IX. The AO-OCT imaging area ($0.6 \times 0.6\ \text{mm}^2$) is illustrated by the

green dashed square. The CCR AO-OCT system was built at the University of California Davis. Details were described in our previous publications.^{19,20} Briefly, the OCT light source operates at 836 nm with 112 nm spectral bandwidth (Superlum, Ireland), allowing theoretical axial resolution of $2.5\ \mu\text{m}$ in the retina. The same light serves as the beacon for wavefront sensing in the AO subsystem that uses a 97-actuator membrane magnetic deformable mirror from ALPAO as wavefront corrector.²⁰ A pupil diameter of 6.7 mm was used to allow for imaging with theoretical lateral resolution of $3\ \mu\text{m}$ when AO correction is optimized. Light reflected from the sample is combined with the light from the reference mirror and then sent to a spectrometer where the CCD line detector (AViiVA™ SM2, e2v) is located and acquires the OCT spectrum at 18,000 axial scans per second. The optical components of the spectrometer consist of an

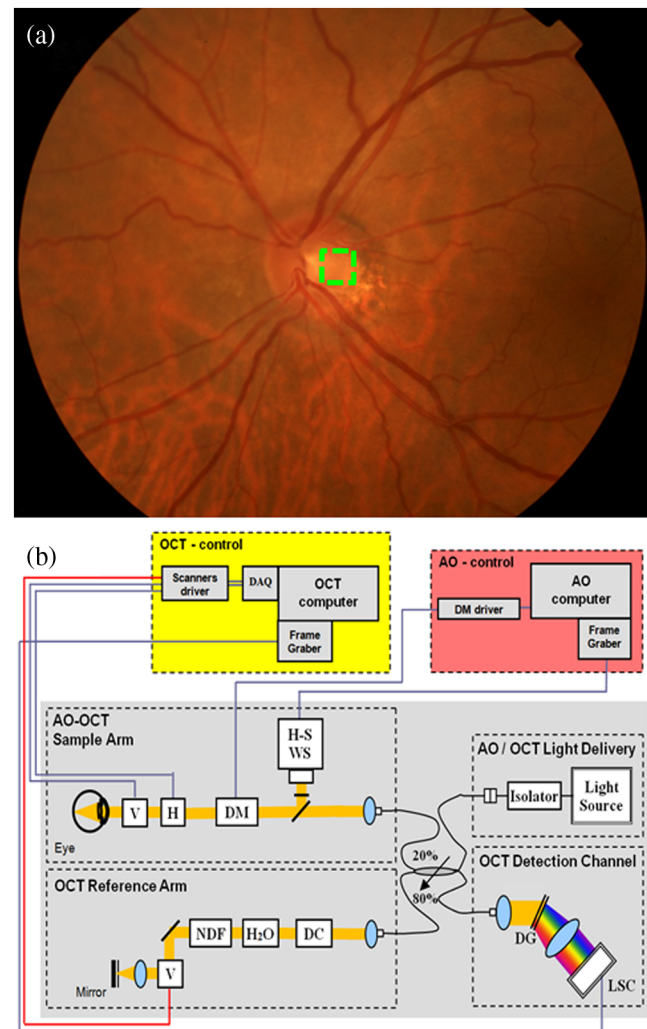


Fig. 1 (a) Color fundus photograph of 60-year-old healthy volunteer's left eye marked with an AO-OCT imaging area, $0.6 \times 0.6\ \text{mm}^2$ at the optic nerve head. (b) Schematic of the optical and electronic components of complex conjugate artifact-free AO-OCT system with the reference arm pivot offset phase-shifting method. Black contours represent fibers and yellow contours represent free-space OCT light paths. V = vertical and H = horizontal scanner; DM = ALPAO deformable mirror; H-S WS = Hartmann-Shack wavefront sensor; NDF = neutral density; H₂O = cuvet with water (to compensate the eye's material dispersion); DC = dispersion compensation (prism pairs); DG = diffraction grating; LSC = line scan camera (SM2, e2v); DAQ = data acquisition card.

achromatic objective collimator, a 1200 line/mm volume holographic diffraction grating, and an $f = 100$ mm objective lens. A bite-bar and a forehead-rest assembly have been mounted on a motorized X - Y - Z translation stage to reduce head motion and allow precise positioning of the subject's eye pupil. A computer-driven (liquid crystal display) target guided the subject's fixation during ONH imaging.

We have recently evaluated three different methods of generating phase shifts between consecutive A-scans allowing reconstruction of the complex spectral fringe pattern in a standard Fd-OCT spectrometer-based instrument with a complementary metal oxide semiconductor (CMOS) high-speed line camera.³ We could not implement the phase shifting method into the AO-OCT sample arm as it would require changes to the sample arm design and would negatively impact AO system performance. Thus, we decided to implement the reference arm mirror-based phase shifting technique^{3,21} in AO-OCT because it provides availability to choose the lateral scanning range and pattern of the imaging beam while keeping a constant phase shift between consecutive A-scans. The reference arm scanning mirror pivot position was shifted in a diagonal direction at a 45-deg angle between the incident beams to generate appropriate constant phase shifts. Scanning range and speed of that mirror were synchronized with the sample arm scanning mirrors. Figure 1(b) shows a schematic of the CCR AO-OCT system with phase shifting at the galvo-scanner located in the reference arm.

The following equation describes the OCT B-scan signal with phase shifts:

$$I(k, t) = \sum_z I_{(z)}(k) \cos\{\varphi_{\text{sr}}[x(t), z] + \varphi_{\text{shifting}}(t) + \varphi_0\}, \quad (1)$$

where k is a wave number, $I_{(z)}(k)$ is an interference intensity, $\varphi_{\text{sr}}(x, z)$ is the phase term between the sample and reference, $\varphi_{\text{shifting}}(t)$ includes phase shifts by phase modulation with proposed methods and object motion, and φ_0 denotes an initial phase. In order to reconstruct the complex spectral fringe pattern, the Fourier transform was applied in the interference fringe $I(k, t)$ along time, i.e., the transverse axis.²² In addition, we employed a band-pass filtering algorithm to enhance image quality by suppressing spurious frequency values. The following inverse Fourier transform of the filter output produced the complex representation of the acquired OCT spectral signal. Finally, inverse Fourier transform of the complex representation toward k generated the mirror artifact-free Fd-OCT image. Details of reconstruction algorithms are explained elsewhere.³ As addressed in our previous publication,³ there are intensity fluctuations along the B-scan when using the reference arm pivot offsetting method. We predicted that phase modulation by pivot-offsetting scanning^{23,24} at the reference arm caused additional phase noises. In order to alleviate this drawback, we added dynamic background (DC) subtraction along B-scans in our postprocessing procedure instead of using conventional DC (averaging B-scans) subtraction. In this method the amplitude of the DC spectrum value for each A-scan is adjusted to optimize DC subtraction.

Unlike swept-source OCT,⁷ spectrometer-based Fd-OCT systems suffer from large sensitivity drops when increasing the distance between the sample location and the zero path length difference position. The sensitivity roll-off of the AO-OCT system was approximately 30 dB at 2.8 mm path length difference between the sample and the reference arm.

The exposure time of the CCD line detector at the measurement was approximately 55 μs . In order to measure the maximum suppression ratio (SR), pivot offsetting scanning of the reference mirror generated half π phase shifts ($\Delta\varphi = 0.5\pi$) between consecutive A-scans. The maximum suppression of the complex conjugate artifact is approximately 23 dB for a paperboard used as the sample. Note that the measured SR value was the mean suppression of 20 axial scans.

3 Results and Discussion

Two AO-OCT cross-sectional images within one volume data set are shown in Fig. 2, where the 0.6 mm lateral scan size of the image consisted of 560 A-scans. The acquisition time of one volume of the data is approximately 3.3 s. Figure 2(a) and 2(c) shows standard processed AO-OCT images at the edge of the optic disc and the center of the disc cup, respectively. Notice that the ONH is positioned at the zero path difference line, and therefore, overlapping real and mirror images are visible. The reconstructed B-scans, after applying the complex conjugate removal algorithm to the AO-OCT data, are shown in Fig. 2(b) and 2(d). Lamellar beams have a highly reflective OCT signal (red dashed arrow). According to Fig. 2, *in vivo* CCR

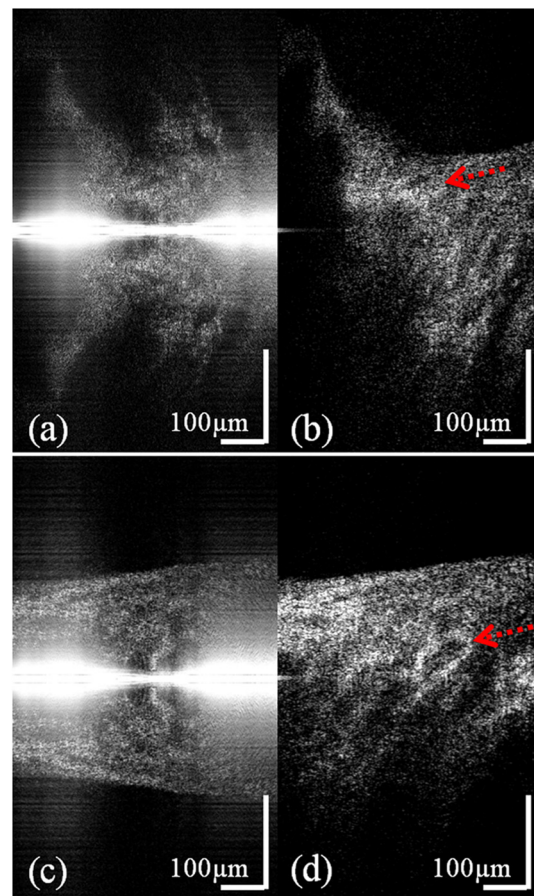


Fig. 2 *In vivo* human optic nerve head images from a single volumetric scan before and after complex conjugate artifact removal. The lateral scanning size is 0.6 mm. (a) and (c) Standard AO-OCT images overlapped with real and mirror artifact images; (b) and (d) Reconstructed images after complex conjugate artifact removal from (a) and (c). Red dashed arrows point to lamellar beams. A combined (before and after complex conjugate artifact removal) of AO-OCT volumetric data ($0.6 \times 0.6 \text{ mm}^2$) can be found in Video 1. (Video 1, MOV, 3 MB) [URL: <http://dx.doi.org/10.1117/1.JBO.17.12.126005.1>].

images with the implemented method showed sufficient artifact removal, with the maximum achievable mirror artifact suppression of 22 dB for this acquisition scheme and the ONH structure. Note a strong zero path-length difference artifact is present on the middle of the left images. It is due to the fact that a simple DC removal technique is not sufficient to compensate for varying DC levels. This DC level variation is challenging to eliminate if the reference arm scanning mirror is used, and here, this artifact is removed by the dynamic background subtraction. A movie of the volumetric scan acquired over $0.6 \times 0.6 \text{ mm}^2$ before and after the complex conjugate removal is attached in this article (Video 1).

The reconstructed AO-OCT B-scan image, Fig. 3(a), from the same volumetric scan with Fig. 2 indicates scan depths (marked yellow dots) of 56, 108, and $145 \mu\text{m}$ below the anterior lamina surface (marked red dots). We selected the top surface of lamina cribrosa from Video 2 where an *en face* projection showed an entire lamina beam structure in a single plane. Figure 3(b) shows a volumetric feature of laminar beam networks over depth ranges between 56 and $145 \mu\text{m}$ from the top lamina surface. As explained above, there was little remaining of zero path length difference line artifact in the edge due to a strong autocorrelation value of the raw AO-OCT data. Note that *en face* visualizations in this article were produced by Gaussian averaging of 15 axial sections, where the separation between each *en face* slice is $\sim 1.3 \mu\text{m}$. In addition, transparency and contrast of the volumetric view were adjusted manually for better visualization.

Figure 4 shows *en face* views of lamina cribrosa pores at different depth locations after removing complex conjugate artifacts shown in Fig. 2. The attached movie shows depth sections of the lamina area from an anterior to a posterior direction (Video 2). This fly-through movie includes approximately $350 \mu\text{m}$ depth information where lamina beam networks can be reliably quantified within an approximately $160 \mu\text{m}$ depth range from the acquired subject's data set. Three frames of the movie are demonstrated in Fig. 4, and the depth locations of the *en face* planes are marked in Fig. 3(a), 56, 108, and $145 \mu\text{m}$ below the top of the anterior lamina structure. Notice that the pore size varies at different *en face* depth views of the three-dimensional lamina structure.

Figure 4(d)–4(f) shows manually segmented eight lamina pores and calculated pore areas using ImageJ (National

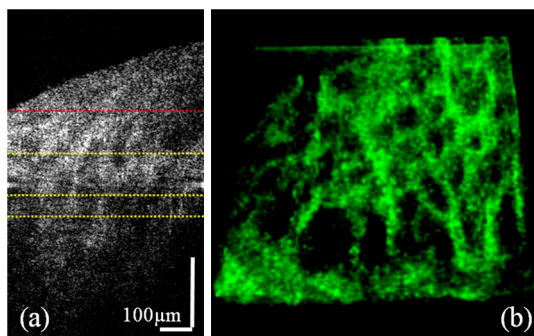


Fig. 3 (a) A mirror artifact-free AO-OCT B-scan image from the same volumetric scan as Fig. 2. The red dotted line marks the top surface of lamina cribrosa and yellow dotted lines indicate depth locations of 56, 108, and $145 \mu\text{m}$ below the anterior lamina surface. (b) A volumetric feature of laminar beam networks over depth ranges between the top and the bottom yellow dotted lines of the CCR AO-OCT data. The $x-y$ scanning size is $0.6 \times 0.6 \text{ mm}^2$.

Institutes of Health, Bethesda, Maryland) from green dotted regions of Fig. 4(a)–4(c), respectively. An observer selected eight pores of the images located over the interior to the exterior lamina. Notice that variable sizes of pores were selected depending on the locations along the transversal axis. For comparison, the histological result of a normal human eye showed that pores were larger in the peripheral region than in the center of the lamina cribrosa.²⁵

Mean pore areas quantified in our analysis of eight lamina pores at three depth locations from Fig. 4(d)–4(f) are 3642, 4260, and $4396 \mu\text{m}^2$, respectively. This result shows good agreement with the histology data (mean: $4000 \pm 1000 \mu\text{m}^2$) of human normal donor eyes.²⁵ We expect the lamina pore size measurement at multiple depth cross-sections to be essential for understanding changes of the structure caused by diseases or aging. Our reason is that the size of pores is diverse transversely in the same *en face* plane²⁵ and axially in depth.²⁶ Ultimately, the *in vivo* volumetric analysis of the lamina structure is optimal to investigate that the laminar beam networks become compressed or collapsed in advanced stages of glaucoma according to a previously published article.²⁷

In this study, we measured the lamina pore geometry from cross-sectional views of the imaging plane. There may be some discrepancies between the average pore sizes measured from microscope images with lamina samples prepared by cutting the same depth from the lamina surface and *in vivo* AO-OCT images. The reason is that the anterior laminar surface in human subjects is elevated as shown in Fig. 3(a) of this manuscript and Fig. 2 of the previously published article.²⁸ Therefore, without compensation of this elevation, pore measurement from a single cross-sectional image may contain measurement errors of actual pore size. As a further investigation, an image-flattening procedure in postprocessing for the *in vivo* imaging is necessary for the precise measurement of the elevated lamina structure.

Note that in our studies two trained operators used a manual drawing toolbox to segment pore boundaries at two different projection views from a three-dimensional fly-through movie. This approach provides “structure from motion” and can minimize measurement errors and provide reliable assessment of the pore structure based on the acquired image quality. The operators tried to delineate the inner side of pores (more toward the darker region than the brighter area) which might cause a slight underestimate of the actual pore size. However, the measurement difference of an average pore size for intraoperator and interoperator repeatability was less than 5%.

The signal-to-noise ratio (SNR) of *en face* lamina pore images in this article may be lower than that of the previous published AO-SLO images.^{13,14} The difference between these two types of images is that the *en face* images shown in our AO-OCT study are from a single volumetric scan with depth information (approximately $350 \mu\text{m}$ in this experiment) while the lamina pore images in the previous article with AO-SLO were produced by averaging over 30 frames of a single *en face* plane. Note that AO-SLO provides the reflectance image, and averaging frames significantly improves the SNR. The OCT, however, uses a coherence detection scheme, so speckle noise is present everywhere in the single acquired image. The speckle pattern is especially distinct when zooming on small structures. As already explained above, *en face* images in this manuscript were produced by Gaussian averaging of 15 sections in order to enhance SNR of the images

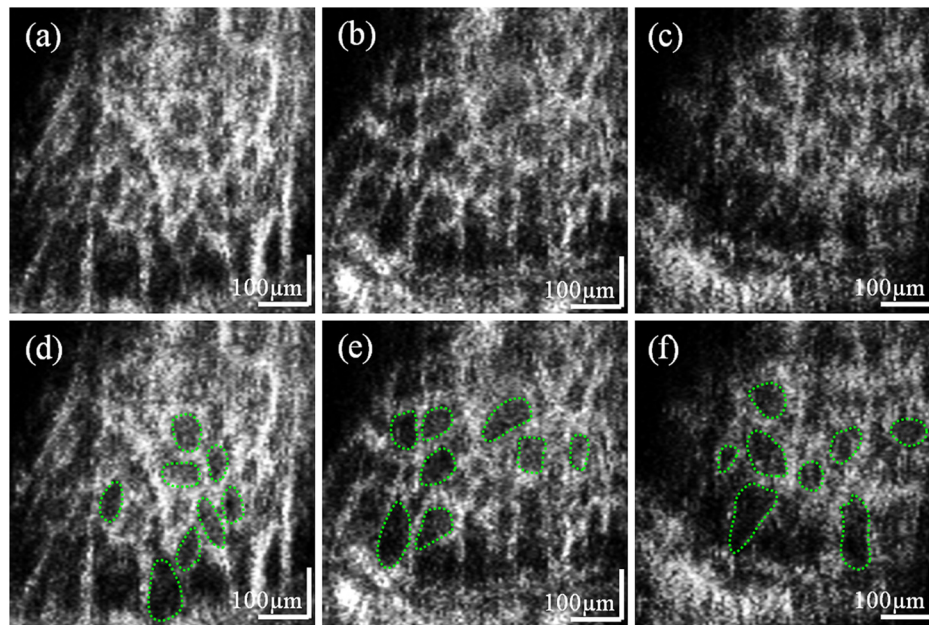


Fig. 4 *In vivo en face* view of the lamina cribrosa and pores at different depth locations, (a) 56 μm , (b) 108 μm , and (c) 145 μm , from the anterior lamina surface. Eight green dotted lamina pores of (d), (e), and (f) were selected to measure lamina pore areas as well as segmented from (a), (b), (c), respectively. Video 2 (MOV, 4 MB) [URL: <http://dx.doi.org/10.1117/1.JBO.17.12.126005.2>] shows C-scan (*en face*) fly-through from anterior to posterior, reconstructed from the same volumetric scan with CCR processing.

and to reduce speckle contrast by averaging multiple planes in depth.

For further enhancement of image quality for AO-OCT, averaging multiple volumetric data with fast acquisition can improve the SNR of our AO-OCT images and reduce speckle noises. Nevertheless, even this limited resolution depth information from the CCR AO-OCT data may allow analysis of *in vivo* three-dimensional pore geometry opening the door for novel methods of monitoring progression in glaucoma. Further improvement in AO correction of ONH structures can also improve resolution of lamina pore imaging.

4 Conclusions

We have implemented a reference arm phase shifting method to an AO-OCT system to achieve CCR imaging for *in vivo* human ONH and lamina cribrosa. The reconstructed mirror artifact-free images were acquired with high sensitivity of the lamina structure because it was possible to place the sample near the zero path length difference position. In addition, the achieved maximum suppression ratio of the complex conjugate mirror image is 22 dB for this lamina cribrosa imaging. We also included dynamic background subtraction in order to compensate for the background intensity variations over cross-sectional scans. The AO-OCT CCR method permits visualization of three-dimensional lamina morphology with high sensitivity and resolution (3 μm axially and 3 μm laterally). It can be used to quantify the area or volume of the lamina pores. This instrumentation may be beneficial in clinical studies requiring measurement of shape parameters of lamina pores and a nearest neighbor distance of each pore with glaucoma patients.

Acknowledgments

The authors thank Steven M. Jones and Scot S. Olivier from the Lawrence Livermore National Laboratory for helping with implementation of AO-OCT at University of California,

Davis. This research was supported by the National Eye Institute (EY 014743) and Research to Prevent Blindness.

References

1. D. Huang et al., "Optical coherence tomography," *Science* **254**(5035), 1178–1181 (1991).
2. M. Wojtkowski et al., "In vivo human retinal imaging by Fourier domain optical coherence tomography," *J. Biomed. Opt.* **7**(3), 457–463 (2002).
3. D. Y. Kim, J. S. Werner, and R. J. Zawadzki, "Comparison of phase-shifting techniques for in vivo full-range, high-speed Fourier-domain optical coherence tomography," *J. Biomed. Opt.* **15**(5), 056011 (2010).
4. M. Wojtkowski et al., "Full range complex spectral optical coherence tomography technique in eye imaging," *Opt. Lett.* **27**(16), 1415–1417 (2002).
5. Y. Yasuno et al., "Simultaneous B-M-mode scanning method for real-time full-range Fourier domain optical coherence tomography," *Appl. Opt.* **45**(8), 1861–1865 (2006).
6. B. Hofer et al., "Dispersion encoded full range frequency domain optical coherence tomography," *Opt. Express* **17**(1), 7–24 (2009).
7. A. H. Dhalla, D. Nankivil, and J. A. Izatt, "Complex conjugate resolved heterodyne swept source optical coherence tomography using coherence revival," *Biomed. Opt. Express* **3**(3), 633–649 (2012).
8. M. Wojtkowski et al., "Ultrahigh-resolution, high-speed, Fourier domain optical coherence tomography and methods for dispersion compensation," *Opt. Express* **12**(11), 2404–2422 (2004).
9. N. V. Swindale et al., "Automated analysis of normal and glaucomatous optic nerve head topography images," *Invest. Ophthalmol. Vis. Sci.* **41**(7), 1730–1742 (2000).
10. B. Fortune et al., "Idiopathic bilateral optic atrophy in the rhesus macaque," *Invest. Ophthalmol. Vis. Sci.* **46**(11), 3943–3956 (2005).
11. G. A. Cioffi, "Ischemic model of optic nerve injury," *Trans. Am. Ophthalmol. Soc.* **103**, 592–613 (2005).
12. G. Wollstein, D. F. Garway-Heath, and R. A. Hitchings, "Identification of early glaucoma cases with the scanning laser ophthalmoscope," *Ophthalmol.* **105**(8), 1557–1563 (1998).
13. A. S. Vilupuru et al., "Adaptive optics scanning laser ophthalmoscopy for *in vivo* imaging of lamina cribrosa," *J. Opt. Soc. Am. A* **24**(5), 1417–1425 (2007).

14. K. M. Ivers et al., "Reproducibility of measuring lamina cribrosa pore geometry in human and nonhuman primates with *in vivo* adaptive optics imaging," *Invest. Ophthalmol. Vis. Sci.* **52**(8), 5473–5480 (2011).
15. T. Akagai et al., "*In vivo* imaging of lamina cribrosa pores by adaptive optics scanning laser ophthalmoscopy," *Invest. Ophthalmol. Vis. Sci.* **53**(7), 4111–4119 (2012).
16. M. Pircher, E. Götzinger, and C. K. Hitzenberger, "Dynamic focus in optical coherence tomography for retinal imaging," *J. Biomed. Opt.* **11**(5), 054013 (2006).
17. V. J. Srinivasan et al., "Ultrahigh-speed optical coherence tomography for three-dimensional and en face imaging of the retina and optic nerve head," *Invest. Ophthalmol. Vis. Sci.* **49**(11), 5103–5110 (2008).
18. R. Inoue et al., "Three-dimensional high-speed optical coherence tomography imaging of lamina cribrosa in glaucoma," *Ophthalmol.* **116**(2), 214–222(2009).
19. R. J. Zawadzki et al., "Cellular resolution volumetric *in vivo* retinal imaging with adaptive optics-optical coherence tomography," *Opt. Express* **17**(5), 4084–4094 (2009).
20. R. J. Zawadzki et al., "Integrated adaptive optics optical coherence tomography and adaptive optics scanning laser ophthalmoscope system for simultaneous cellular resolution *in vivo* retinal imaging," *Biomed. Opt. Express* **2**(6), 1674–1686 (2011).
21. M. Szkulmowski et al., "Flow velocity estimation by complex ambiguity free joint spectral and time domain optical coherence tomography," *Opt. Express* **17**(16), 14281–14297 (2009).
22. B. Baumann et al., "Full range complex spectral domain optical coherence tomography without additional phase shifters," *Opt. Express* **15**(20), 13375–13387 (2007).
23. L. An and R. K. Wang, "Use of a scanner to modulate spatial interferograms for *in vivo* full-range Fourier-domain optical coherence tomography," *Opt. Lett.* **32**(23), 3423–3425 (2007).
24. R. A. Leitgeb et al., "Complex ambiguity-free Fourier domain optical coherence tomography through transverse scanning," *Opt. Lett.* **32**(23), 3453–3455 (2007).
25. J. B. Jonas et al., "Morphometry of the human lamina cribrosa surface," *Invest. Ophthalmol. Vis. Sci.* **32**(2), 401–405 (1991).
26. R. L. Radius and M. Gonzales, "Anatomy of the lamina cribrosa in human eyes," *Arch. Ophthalmol.* **99**(12), 2159–2162 (1981).
27. H. A. Quigley et al., "Optic nerve damage in human glaucoma. II. The site of injury and susceptibility to damage," *Arch. Ophthalmol.* **99**(4), 635–649 (1981).
28. Y. Agoumi et al., "Laminar and prelaminar tissue displacement during intraocular pressure elevation in glaucoma patients and healthy controls," *Ophthalmol.* **118**(1), 52–59 (2011).